

Lecture 3

Micro Imaging and Quantitative XRF micro Analysis

3.1 Basic Equations

The schematic representation of the interaction between the incident x-ray and the sample is shown in figure 3.1. The incident x-rays with a wavelength λ , which irradiates the sample, are attenuated and generate scattered x-rays (Rayleigh scattering and Compton scattering) and fluorescent x-rays, accompanied by the generation of photoelectrons. When the sample is a pure element i , according to the Beer-Lambert law, the intensity of the transmitted x-rays with wavelength λ , $I(\lambda)$, is given by:

$$I(\lambda) = I_0(\lambda) \exp\{-\mu_i(\lambda)\rho_i t\} \quad (3.1)$$

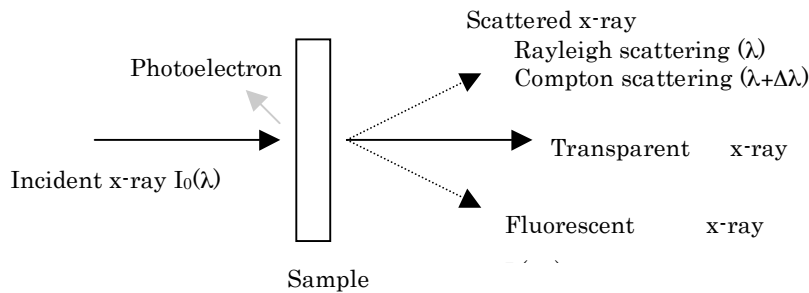


Figure 3.1. The schematic drawing of the interaction between x-ray and the materials.

where the $I_0(\lambda)$ is the intensity of the incident x-ray with wavelength λ , $\mu_i(\lambda)$ is the effective mass attenuation coefficient of element i for incident wavelength λ , ρ_i is the density of element i , and t is the thickness of the sample. The total effective mass attenuation coefficient $\mu(\lambda)$ of a multi-element specimen is given by the simple relationship

$$\mu(\lambda) = \mu_1(\lambda)W_1 + \dots + \mu_n(\lambda)W_n \quad (3.2)$$

where W_1, \dots, W_n are the weight fraction of components.

In the experimental configuration shown in figure 3.2., the intensity that reaches the depth of z , represented by $I(\lambda, z)$ is given by

$$I(\lambda, z) = I_0(\lambda) \exp\left\{-\mu(\lambda)\rho \frac{z}{\sin \phi}\right\} \quad (3.3)$$

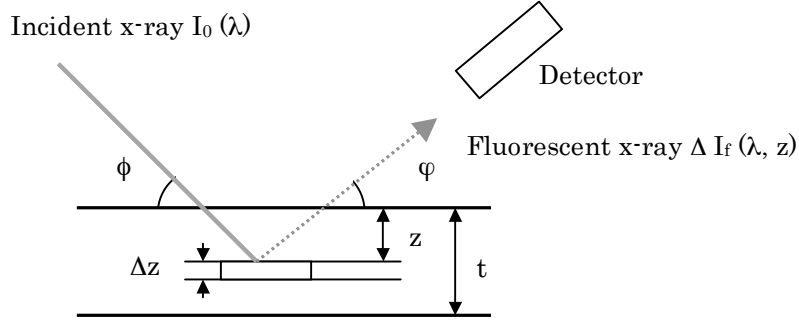


Figure 3.2. Schematic representation of the experimental configuration of the incident x-ray, the sample and the detector.

where ϕ is the incidence angle and ρ is the density of the sample. The intensity of primary fluorescent x-ray generated in the sample between the depth of z and $z + \Delta z$, represented $\Delta I_f(\lambda, z)$ is given by

$$\begin{aligned} \Delta I_f(\lambda, z) &= P_i \mu_i(\lambda) W_i \rho \{I(\lambda, z) - I(\lambda, z + \Delta z)\} \\ &= P_i I(\lambda, z) \left\{ \mu_i(\lambda) W_i \rho \frac{\Delta z}{\sin \phi} \right\} \end{aligned} \quad (3.4)$$

where P_i is the probability that a characteristics x-ray line of element i is emitted, which is determined mainly by the ionization cross section and the fluorescence yield. The intensity of the primary fluorescent x-ray at the surface of the sample $\Delta I_f(\lambda)$ is given by

$$\begin{aligned} \Delta I_f(\lambda) &= \Delta I_f(\lambda, z) \times \exp\left\{-\mu(\lambda_f) \rho \frac{z}{\sin \phi}\right\} \\ &= P_i I_0(\lambda) \mu_i(\lambda) W_i \rho \frac{\Delta z}{\sin \phi} \exp(-\bar{\mu} \rho z) \end{aligned} \quad (3.5)$$

where

$$\bar{\mu} = \frac{\mu(\lambda)}{\sin \phi} + \frac{\mu_f(\lambda_f)}{\sin \phi} \quad (3.6)$$

λ_f is the wavelength of the fluorescence x-ray, and ϕ is the take-off angle of the fluorescent x-ray detector. Therefore the total primary x-ray fluorescence yield I_f from a sample of a thickness t is given by

$$\begin{aligned}
I_f(\lambda) &= \int_0^t \Delta I_f(\lambda) dz \\
&= P_i I_0(\lambda) \mu_i(\lambda) W_i \frac{1}{\sin \phi} \{1 - \exp(-\bar{\mu} \rho t)\} \frac{1}{\mu} \quad (3.7)
\end{aligned}$$

In this study, the samples are thin sections and their major constituents are light elements. Therefore the magnitude of $\mu \rho t$ is small and the above equation can be approximated as

$$I_f(\lambda) = P_i I_0(\lambda) \mu_i(\lambda) W_i \rho \frac{t}{\sin \phi} \propto W_i \rho t \quad (3.8)$$

Under this approximation, the fluorescent x-ray intensity from each element is proportional to the incident x-ray intensity and to the area density of the element $W_i \rho t$. The fluorescent x-ray intensity that reaches the solid state detector $I_f'(\lambda)$ is given by

$$I_f'(\lambda) = C(\lambda) C_i I_f(\lambda) \quad (3.9)$$

where $C(\lambda)$ is the constant that is determined by the geometrical parameters of the set-up instruments such as the solid angle to the detector and the path of the incident x-ray, and C_i is the constant determined by the attenuation coefficient of the path of the fluorescent x-ray about element i , which includes Be-window of the Si detector. $C(\lambda)$ and C_i are constants under the same experimental condition.

The fluorescent x-ray yield that reaches the detector is directly proportional to the peak areas $A_{peak i}$ of element i in the XRF spectra.

$$A_{peak i} = C' I_f'(\lambda) \quad (3.10)$$

where C' is the efficiency of the detector. Therefore the below equation can be derived from (3.8), (3.9), and (3.10).

$$A_{peak i} = \frac{1}{\sin \phi} C' C(\lambda) C_i P_i I_0(\lambda) \mu_i(\lambda) \rho_i' \quad (3.11)$$

where

$\rho_i' = W_i \rho t$ = the area density of the element i .

C_i , P_i and $\mu_i(\lambda)$ can be obtained from the existing database and handbooks [1,2]. $I_0(\lambda)$ was monitored by an ionization chamber. The product of C' and $C(\lambda)$ can be calculated by comparing the area density of element i and the peak area obtained from the reference sample, for which the area density of element i is already-known. It is thus possible to calculate the

area densities of all elements from the XRF spectra because the product of C' and $C(\lambda)$ is independent of the elements. In this study, thin pure metal films whose thicknesses are known were used as the reference standards. After the determination of C' and $C(\lambda)$, the local area densities of all elements in the biological sample can be directly calculated from the measured XRF spectra.

3.2 Development of Computer Programs for Quantitative XRF Analysis

3.2.1. Objective

This chapter describes a computer code that has been developed for the quick processing of XRF spectra and quantification of the trace elements. This code can be used to investigate several important neurodegenerative diseases such as Alzheimer's disease (AD), Parkinson's disease (PD), Parkinsonism dementia complex (PDC) and amyotrophic lateral sclerosis (ALS), as well as to investigate basic biological samples in order to study changes in cells due to the incorporation of foreign metal elements.

The elemental area density can be calculated from the XRF spectra according to the equations described in the previous section. The typical constituents detected in the XRF analysis of biomedical samples are P, S, Cl, K and Ca, which are the main components of a living tissue. These peaks in the spectra overlap with each other making difficult to decompose the peaks and calculate their areas accurately. The example of XRF spectrum is shown in figure 3.3, in which P, S, Cl and Ar peaks are strongly overlapping. In order to analyze such peaks appearing in spectra, many algorithms for background identification and peak discrimination have been reported in many fields to obtain quantitative information, but various limitations exist tying each algorithm to specific spectral shapes [3]. The main purpose of these programs is to automate the numerical processing in obtaining correct quantitative data in the following three aspects [4]:

1. identification of background intensity
2. recognition of existing peaks
3. evaluation of positions and intensities

Few programs are available for the quantification using synchrotron radiation XRF. In this study, we originally designed the program that features the semi-automatic peak shape, energy and yield. It also includes graphical user interface and quantification procedures. In addition to the requirements described above, this program also has the following properties:

4. capability to analyze the spectra containing high noise
5. high flexibility to meet experimental conditions
6. simple and fast quantification from the peak areas
7. integration of multiple data

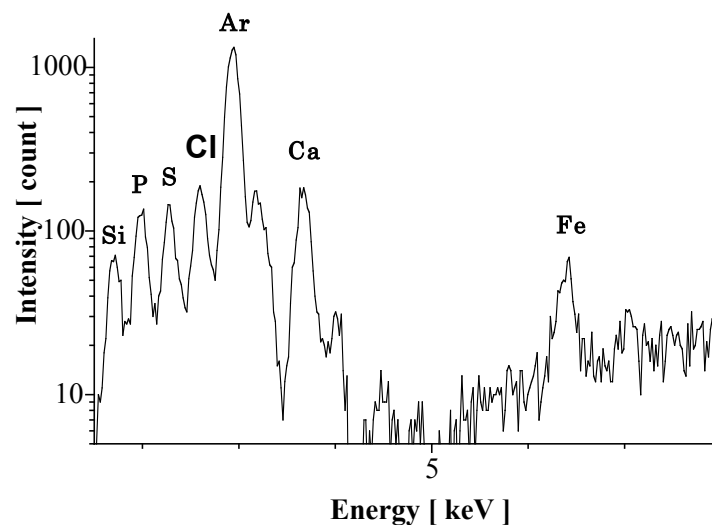


Figure 3.3. The example of the XRF spectrum obtained from a biological sample. The fluorescent peaks from Si, P, S, Cl and Ar contents are strongly overlapping.

The biomedical samples generally contain heavy elements at low concentration, and the elemental distributions are not homogeneous. Therefore the spectra are not so clear as compared to those from minerals. High flexibility to the change of path length or experimental atmosphere is also important because we use several different incident energies according to the experimental purpose, and some of the experiments are performed in air, others in vacuum. Features 6 and 7 are required to process large data obtained from large number of samples. The accumulation of the quantitative information is essential because the statistical accuracy is important in evaluating the biological function such as the differentiation of mouse embryonic stem cells or cell death in neurodegenerative disorders from the aspect of the elemental conditions. In these studies, it will be necessary to understand the extent of residues and to obtain the average data as criteria. Recently the number of samples is increasing due to the improvement of experimental efficiency and the increase of objective cases. The signification of systematic and fast processing of data is enhanced in accordance with the increase of samples. On the other hand, feature 2 is omitted in our program. In x-ray spectroscopy peak finding is usually not the crucial state of analysis because the peak locations are known beforehand [5].

3.2. 2. Algorithm And Basic Equations For The Spectrum Analysis And Quantification

This program is written in Visual Basic version 6. The quantification of trace elements is performed in the following procedures. First, the analysis of the spectra obtained from reference samples are carried out. The reference samples are metal thin films whose thicknesses are already known. In this study, we analyzed pure films of Ti, Cr, Mn, Fe, Co, Ni and Cu. In this process, the peaks are fitted using the least squares method by varying the width, position and height of the peak after the background is estimated from the untreated spectra. The relations between the fluorescent intensity and the concentration are determined by comparing the peak areas from the samples with different thicknesses. The relation between channel and energy, the width and energy are also determined by comparing the position and the width of different kinds of the samples.

In the next process, the analysis of spectra obtained from autopsy specimens is performed based on the results from reference samples. In this process, only the heights of peaks have to be determined at the beginning because the width and the position have already been determined in the previous process. After the first coarse fitting by modulating the heights, the fine fitting is applied to each single peak in which the width, position and height of the peak are adjusted.

In the last process, the concentrations of the elements in the biomedical specimens are quantified by comparing the peak areas obtained in the second process to those of reference samples obtained in the first process. The algorithm and the basic equation utilized in the program are described detailed in the following section.

3.2.3. Estimation of The Background

Quantitative analysis using XRF spectra requires the removal of the background prior to the estimation of the net area of the peaks. But the sample mass absorption coefficient, which is needed when calculating the background function, depends on the composition of the sample and is originally unknown. Therefore the extraction of the background is generally performed in several numerical ways [6]. In this program, the simple peak clipping approach was applied [7]. In order to process data from numerous spot analysis efficiently, a background approximation must be free of user-adjustable parameters to permit batch processing. The peak clipping approach provides rapid and robust estimation. This method is based on the equation represented by

$$Y_i = \min Y_i, m_i \quad (m_i = Y_{i-1} + Y_{i+1}) \quad (3.12)$$

where Y_i is the count of channel i of the multi channel analyzer, and m_i is the mean of the counts of channel $i-1$ and $i+1$. When the count of a certain channel i is compared to m_i , if Y_i is

larger than m_i , it is replaced with m_i . This procedure is repeated for the selected extent of channels and the projections of spectra are gradually removed. The background of the spectra can be estimated easily by repeating this replacement. The pass count of 2000 is chosen as the default value. Figure 3.4 shows the example of the estimation of the background in XRF spectrum. The solid and dotted lines show the untreated spectrum and the estimated background respectively. The smoothing of the spectra can also be performed if needed.

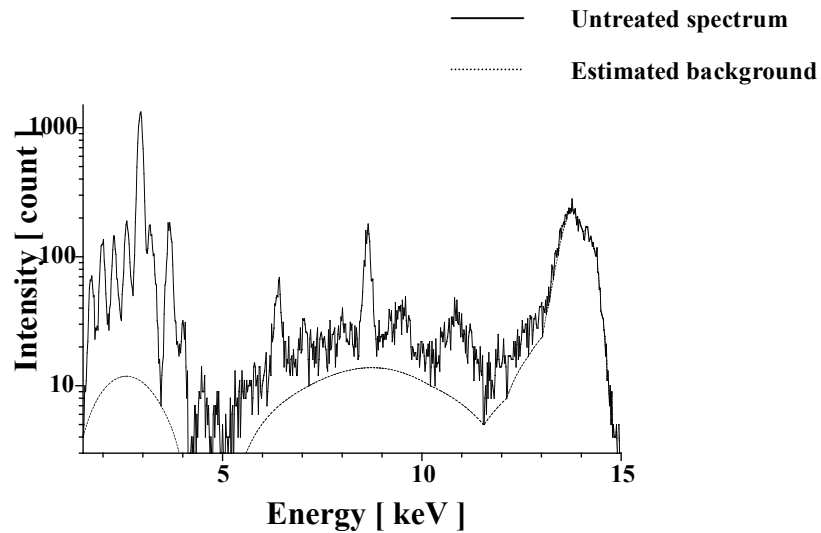


Figure 3.4. Example of the estimation of the background in XRF spectrum obtained by the peak clipping approach.

3.2.4. Single Peak Fitting

Once the background has been evaluated, it is possible to carry out the peak fitting. The peaks are determined by the least squares method. Since the model functions for peak shapes are nonlinear with respect to their parameters, iteration is needed to perform the least squares fitting. The single peaks are fitted as Gaussian functions and are represented by

$$y(x) = H \exp\left\{-\frac{(M-x)^2}{S}\right\} \quad (3.13)$$

where M , S and H determine the position, FWHM (full width at half maximum) and height of the peaks respectively and $y(x)$ is the counts of the fitted peak in channel x . The objective function P is calculated via

$$P = \sum_i \{C(i) - B(i) - y(i)\}^2 \quad (3.14)$$

where $C(x)$ is the experimental counts obtained in channel x , $B(x)$ is the estimated background in channel x and i shows the extent of channels to which the fitting is applied. In this program, the steepest decent method was applied for a non-liner fitting of the peaks. This method modulates the variables of M , S and H as

$$M = M - \frac{\partial P}{\partial M} dA, S = S - \frac{\partial P}{\partial S} dA, H = H - \frac{\partial P}{\partial H} dA \quad (3.15)$$

where dA is the step size. When these equations are directly applied, the absolute of the gradient P changes unstably, and M , S and H often diverge. Therefore, this program employs the modified steepest decent method, in which the variables are defined as

$$M = M - W_M \frac{\partial P}{\partial M} dA, S = S - W_S \frac{\partial P}{\partial S} dA, H = H - W_H \frac{\partial P}{\partial H} dA \quad (3.16)$$

where W_M , W_S and W_H are the weight functions for M , S and H . These weight functions are determined empirically as

$$W_M = \frac{1}{H^2} \exp \frac{2}{S}, W_S = \frac{20}{H}, W_H = \frac{S}{5(1 - 4S^{2.5})} \quad (3.17)$$

These weight functions are then normalized by the absolute value of the vector of (W_M, W_S, W_H) and used for the modulation of the variables. $dA = 1$ is chosen as the default number. The single peak fitting is performed by repeating the equation (3.16) until the objective purpose is minimized.

Figure 3.5 shows the example of the single peak fitting in the XRF spectrum, which was obtained from the reference sample of a Cu thin film. The black solid and dotted lines show the untreated spectrum and the estimated background respectively, and blue dotted line shows the peak obtained by the fitting. It can be seen the fitted Gaussian is well correspondent to the measured spectrum.

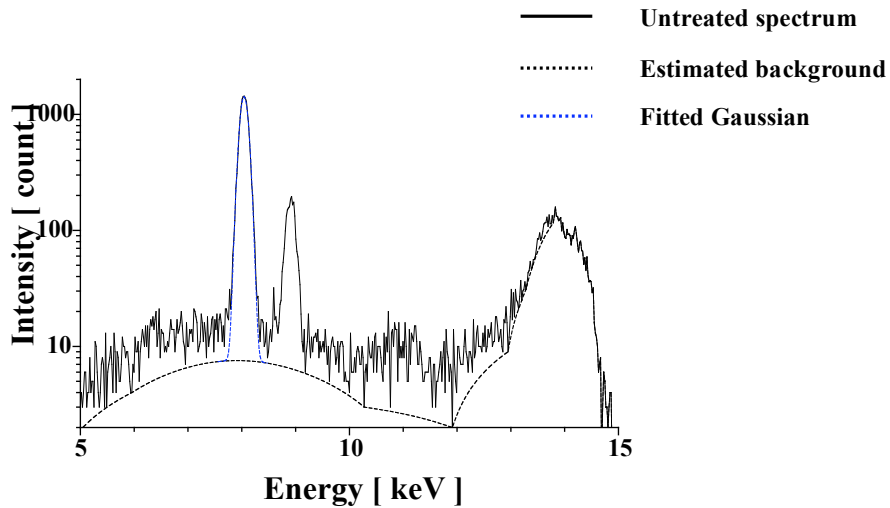


Figure 3.5. Single peak fitting in the XRF spectrum, which was obtained from the reference sample of Cu thin film. It can be seen the fitted Gaussian is well correspondent to the measured spectrum

3.2.5. Derivation of Calibration Curves

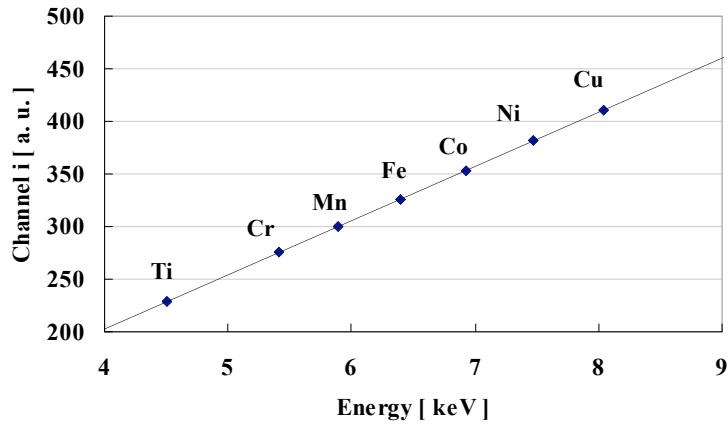
There are the relational expressions between the channel i of the multi-channel analyzer and the x-ray energy E , and between the variable S that determines the FWHM of the peaks and x-ray energy E , which are represented by

$$i = aE + b \quad (3.18)$$

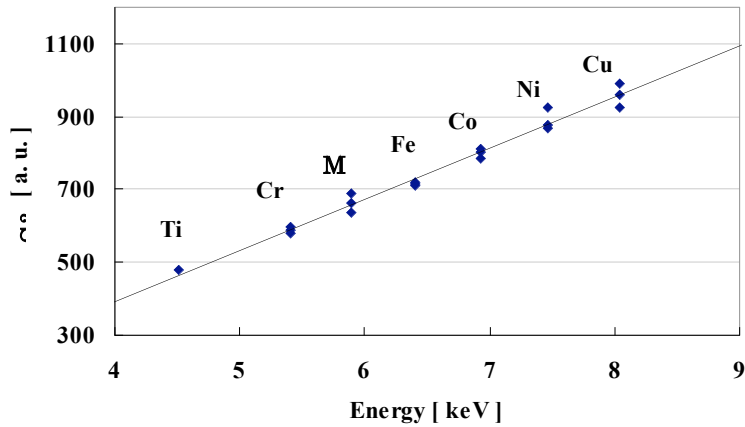
$$S^2 = cE + d \quad (3.19)$$

where a , b , c and d are the variables determined by the properties and configuration of the multi-channel analyzer and the detector [6]. Figure 3.6 (a) and (b) shows the relationships between i and E , and S and E respectively, which were obtained from the analysis using reference samples of Ti, Cr, Mn, Fe, Co, Ni and Cu thin films. Three films whose thicknesses were different (60 – 280 Å) were analyzed for each kind of the elements. The deviations between measured and calculated values were less than 7 % and 1 % for figure 3.6 (a) and (b) respectively.

These expressions are utilized in the multiple peak fitting. Through these relationships, it is possible to determine the position and width of the elemental peaks other than the analyzed reference samples (e.g. P, S, Cl, Ar, K, Ca, Sc, V and Zn).



(a) Relation between channel i and x-ray



(b) Relation between the variable S and x-ray

Figure 3.6. The relationships between the channel i of the multi-channel analyzer and the x-ray energy E , and between the variable S that determines the FWHM of the peaks and x-ray energy E . The results were obtained from the analysis using reference samples of Ti, Cr, Mn, Fe, Co, Ni and Cu thin films

3.2.6. Multiple peak fitting

Based on the position and the width of the peaks obtained in the previous step, the multiple peak fitting is performed to the XRF spectra from the biomedical samples. The peaks are determined by the least squares method and their shapes are represented as Gaussian curves. The single peak is given by

$$y(x) = H \exp\left\{-\frac{(M'-x)^2}{S'}\right\} \quad (3.20)$$

where M' , S' and H determine the position, FWHM and height of the peaks respectively and $y(x)$ is the counts of the fitted peak in channel x . M' and S' are obtained from the equation (3.18) and (3.19) and are not modulated in this process. The objective function P is represented by

$$P = \sum_{k=1}^n \sum_i \frac{1}{\omega_i^2} \{C(i) - B(i) - y_k(i)\}^2 \quad (3.21)$$

where $C(x)$ is the experimental counts obtained in channel x , $B(x)$ is the estimated background in channel x and i shows the extent of channels to which the fitting is applied. Y_k is k th peak applied fitting and n is the number of the peaks. The weight function, w_i , is given by

$$\omega_i = \begin{cases} C(i)-B(i) & (C(i)-B(i) > 10) \\ 10 & \dots \dots \dots \end{cases} \quad (3.22)$$

This factor enables to process the large and small peaks at the same time. The minimum value (=10) is set for this factor not to overestimate the small peaks. Then the valuable H is determined for each fitted peak by the steepest decent method. The valuable H is modulated by

$$H_i = H_i - \frac{\partial P}{\partial H_i} dA, \quad i = 0, 1, \dots, n \quad (3.23)$$

where H_i is the height of i th peak and n is the number of the fitted peaks. Figure 3.7 shows the example of the multiple peak fitting performed in this procedure and the residual between the measured spectra and the sum of the estimated background and peaks. The black solid and dotted lines show the measured spectra and the estimated background respectively. Blue dotted lines show fitted multiple peaks. The overlapping peaks are decomposed appropriately in accordance with the decrease of the objective function.

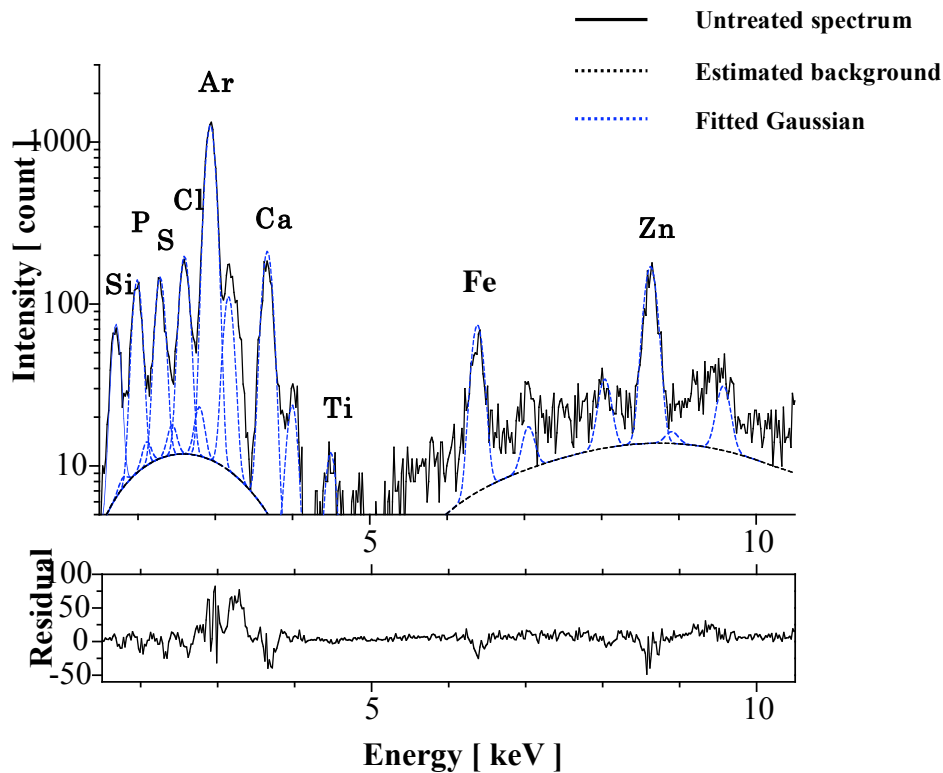


Figure 3.7. The result and the residual of the multiple fitting applied to the XRF spectra obtained from the biomedical sample. The fitting was performed by the steepest decent method modulating the heights of the peaks.

After the first fitting, the further fitting can be applied to each peak in the same procedure as the single peak fitting. The positions, width, height of each peak are further adjusted. Figure 3.8 shows the example of the result of further fitting and the residual. The black solid, dotted lines and blue dotted lines show the measured spectra, estimated background and fitted peaks respectively. It can be seen that the residual has been improved compared to the result from the first fitting. The remained residual is ascribable to the noise and the absorption of fluorescent x-ray in the sample and the path of x-ray.

Once the Gaussians are fitted to all peaks in the XRF spectrum, the net peak areas are obtained for each element. Then the elemental concentrations are calculated according to the equation (3.11).

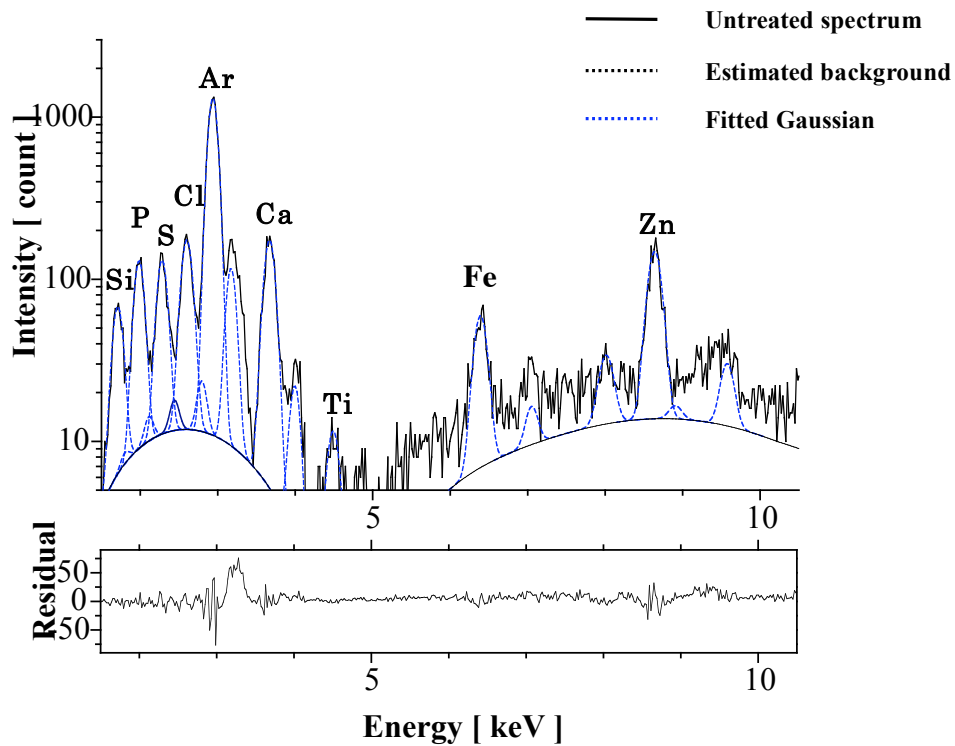


Figure 3.8. The result and the residual of the further fitting applied after the first multiple peak fitting. The heights, position and width of the peaks were adjusted one by one in the same procedure as the single peak fitting. It can be seen that the residual has been improved compared to the result from the first fitting shown in figure 3.7.

3.3. Minimum Detection Limit

If the intensity of fluorescence x-ray is measured under the same conditions, then the matrix effect can be neglected and the relation between the concentration (W_i) and the fluorescent x-ray I_i from element i can be written as follows,

$$I_i = b_{0i} + b_{1i} \cdot W_i. \quad (3.24)$$

Assume now that a reference sample with the element of interest whose concentration is C_s is measured by XRF analysis. If for t seconds the counts of the fluorescent x-ray peak and its background are defined as N_{SP} and N_{SB} respectively, the slope ($\tan \beta$) of the calibration line is given by

$$\tan \beta = \frac{N_{SP} - N_{SB}}{C_s} \quad (3.25)$$

Using the equation (3.19), the equation (3.18) can be written as

$$N_{SP} = N_{SB} + \tan f \tilde{A} C_S. \quad (3.26)$$

For an unknown sample, the concentration of the same element W_i can be derived from the peak and background counts N_P and N_B

$$W_i = \frac{N_P - N_B}{\tan f \tilde{A}} \quad (3.27)$$

The counts in the peak displays Poisson distribution pattern. The standard deviation of the net peak counts " $N_P - N_B$ " is given by:

$$\sqrt{N_P + N_B} \quad (3.28)$$

For the peak to be detectable, the following inequality has to be satisfied.

$$\frac{N_P - N_B}{\sqrt{N_P + N_B}} > u_0 \quad (3.29)$$

where $u_0 > 0$. In the region of the peak where the concentration of the element to be detected is at the minimum detection limit, the values of N_P and N_B are almost equal. Thus, the inequality (3.29) can be written as (3.30)

$$N_P - N_B > u_0 \sqrt{2 \cdot N_B} \quad (3.30)$$

From (3.25), (3.27) and (3.30), the minimum detection limit C_{DL} can be expressed as (3.31)

$$C_{DL} = \frac{u_0 \sqrt{2} \cdot \sqrt{N_B} \cdot C_S}{N_{SP} - N_{SB}} \quad (3.31)$$

For 99 % confidence limit, the minimum detection limit C_{DL} is defined as (3.32)

$$C_{DL} = \frac{3 \cdot \sqrt{N_B} \cdot C_S}{N_{SP} - N_{SB}} \quad (3.32)$$

It is necessary to display the detection time with C_{DL} because the minimum detection limit changes according to the detection time. In order to make C_{DL} small, the value of the background has to be suppressed and the slope of the calibration curve has to be made larger [8].

3.4. Discussion

In this section, the computer program developed for the quantitative XRF analysis for the biomedical samples was introduced. Together with the experiments with XRF spectrum analysis, the program is able to fit accurately complex multiplets. This program provides the effective solution to process the data systematically and robustly and has been successfully used both for stringent spectroscopic studies and for routine analysis of large amounts of data. In the following studies, this program was utilized to consider the correlation between the biological functions and the intracellular trace elements. The concentrations of trace elements deduced using this program showed the stability over a wide range of counting statistics.

There are, however, several points to be considered. For the detailed evaluation of the accuracy and reliability of this program, it is necessary to analyze standard materials and to compare the results with the nominal values. In this study the metal thin films made by the vapor deposition on Mylar film, whose thicknesses were from 60 to 280 Å, were used as the reference samples. But these thicknesses were measured by the crystal oscillator and it is possible that they contain certain errors. These samples should be analyzed complementary by other methods. Furthermore, powerful test of the reliability under the effects of changes in statistics can be made by applying Monte Carlo techniques to simulate spectra of arbitrary intensity [6, 7]. Employing a high-statistics spectrum as the parent probability distribution, low-statistics spectra can be generated.

The absorption of fluorescent x-ray by the sample and the consequent excitation of other elements are not considered in this program. These effects are considered to be small and are neglected because the samples are thin sections and their main constituents are light elements. But in order to reach results with even higher accuracy, it is clear that matrix correction procedures must be adopted individually for the inducing radiation.

3.5. XANES Analysis for Metalloprotein in Biomedical Samples

3.5.1. Principles and Features of Micro-XANES

X-ray absorption fine spectra (XAFS) refers to the oscillatory structure in the x-ray absorption coefficient just above an x-ray absorption edge. It is caused by energy-dependent modulations of photoelectron scattering intensity, which reflects the local atomic structure and chemical information in the analyzed material [9-11]. It provides molecular-level information not previously available using other techniques, such as the species of atoms present and their locations. This information is meaningful in many fields, including material science and biology. The XAFS spectrum is usually divided into the x-ray absorption near-edge structure (XANES) region and the extended x-ray fine structure (EXAFS) region, depending on the strength of photoelectron scattering. The XANES spectrum is represented by the energy region from just below to -50 eV above the absorption edge and serves as a site-specific probe of local charge state, coordination, and magnetic moment of the central absorber [12]. This region is determined by full multiple photoelectron scattering, whereas the EXAFS region reflects single and low-order multiple scattering.

XANES spectra are collected in transmission and fluorescence modes. The spectra are represented as the function of photon energy, which is given by

$$\mu = -\exp \frac{I}{I_0} \quad (\text{transmission mode}) \quad \text{or} \quad \frac{I_f}{I_0} \quad (\text{fluorescence mode})$$

where I_0 , I and I_f are the incident, transmitted and fluorescent x-ray intensities respectively. These first two are measured by ionization chambers and the last by Si(Li) detector. A detailed experimental study confirmed that the fluorescent detection mode yielded essentially the same results as the conventional transmission mode for various iron compounds [13]. Fluorescence detection of XAFS is usually the appropriate mode of detection of x-rays for dilute samples, such as biological samples, because the signal to noise ratio in fluorescence mode is often superior to that in transmission mode. Figure 3.9 shows the examples of the XANES spectra that were obtained from powder reference samples of FeO, Fe₂O₃ and Fe₃O₄. These spectra were recorded in transmission mode. It can be seen that the absorption edge position shifts to the high-energy side according to the increase of the valence of iron.

The importance of XANES analysis is enhanced in accordance with the increase of new synchrotron x-ray sources. The high spatial resolution, sensitivity and the energy tunability are compatible in the analysis using SR and these characteristics can not be obtained in other conventional techniques. So micro-XANES analysis is the one of the most successful application fields of SR spectroscopy and provides unique information on the local atomic

arrangement and the electronic state [14]. The study of the active site of proteins and variations on ligand binding is widely performed in the field of biology, and it is providing very important information for gaining an understanding of the relationship between the protein structure and its function [15]. In this study, the changes in the local chemical structure of iron and zinc binding site, which had been accompanied by the progress of neurodegenerative diseases or the differentiation of mouse ES cells, were investigated by this novel technique.

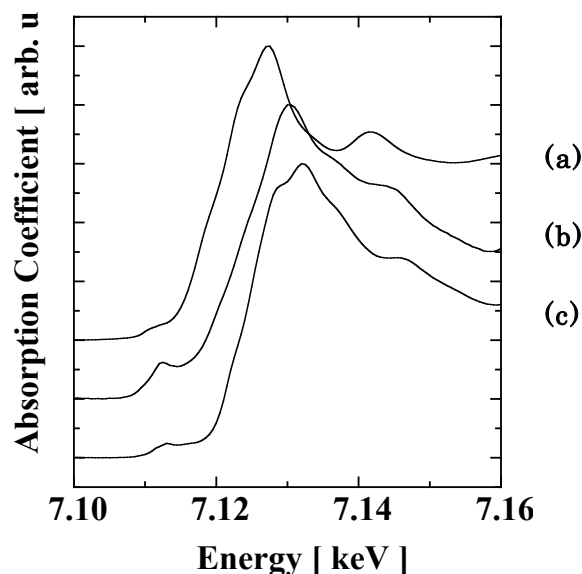


Figure 3.9. The XANES spectra that were obtained from the powder reference samples of FeO, Fe₂O₃ and Fe₃O₄. These spectra were recorded in transmission mode.

3.5.2. Beam Line Set Up and Experimental Instrument

In this study, XANES analysis was carried out in SPring-8 BL39XU. The experimental arrangement was the same as that for the XRF analysis, which is shown in figure 3.10. Micro-XAFS measurement is performed using reflection optics in combination with a double crystal monochromator with a constant exit beam.

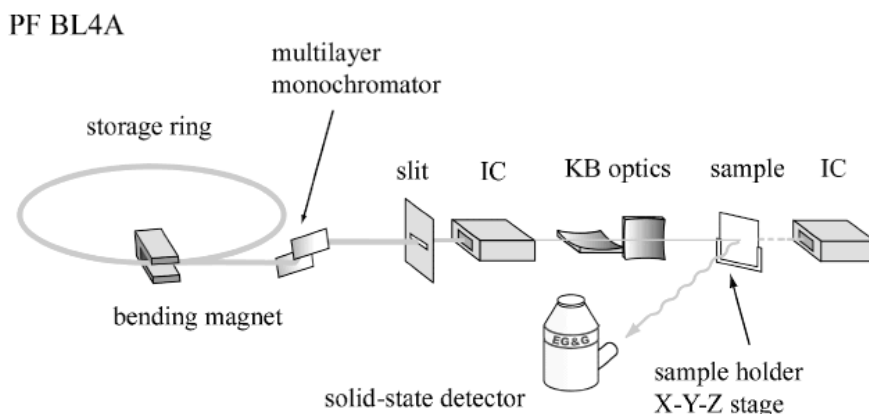


Figure 3.10. The experimental arrangement was carried out in SPring-8 BL39XU.

With the double crystal monochromator, the incident energy can be changed continuously. The combination of fundamental/third harmonics of undulator radiation with the Si (1,1,1) reflection of the monochromator enables an energy range from 5 to 37 keV. The incoming photon flux is maximized at every x-ray energy by synchronous tuning between the undulator gap and the monochromator automatically.

References

1. J.W. Mayer, E. Rimini, “*Ion Beam Handbook for Material Analysis*”, Academic Press, 1977.
2. J. R. Tesmer, M. Nastasi, J.C. Barboe, C.J. Maggiore, J.W. Mayer, “*Handbook of Modern Ion Beam Materials Analysis*”, Materials Research Society, 1995.
3. M.A. Kneen, H.J. Annegarn, *Nucl. Instrum. Meth. Phys. Res. B*, 1996, 109, 209.
4. J.Z. Chu, S.X. Hu, G.Y. Tao, *Chemom. Intell. Lab. Sys.*, 1996, 32, 83.
5. P.A. Aarnio, H. Lauranto, *Nucl. Instrum. Meth. Phys. Res. A*, 1989, 276, 608.
6. B. Vekemans, K. Janssens, L. Vincze, F. Adams, P. van Espen, *Spectrochim. Acta B*, 1995, 50, 149.
7. C.G. Ryan, E. Clayton, W.L. Griffin, S.H. Sie, D.R. Cousens, *Nucl. Instrum. Meth. Phys. Res. B*, 1988, 34, 396.
8. K. Sugihara, K. Tamura, M. Sato, K. Ohno, *X-ray Spectrometry*, 1999, 28, 446.
9. P.M. Bertsch, D.B. Hunter, *Chemical Reviews*, 2001, 101, 1809.
10. C. Bouldin, J. Sims, H. Hung, J.J. Rehr, A.L. Ankudinov, *X-ray Spectrometry*,
11. J.J. Rehr, R.C. Albers, *Rev. Mod. Phys.*, 2000, 72, 621.
12. A.L. Ankudinov, B. Ravel, J.J. Rehr, S.D. Conradson, *Phys. Rev. B*, 1998, 58, 7565.
13. I. Nakai, C. Numako, S. Hayakawa, A. Tsuchiyama, *J. of Trace and Microprobe Techniques*, 1998, 16, 87.
14. A. Iida, *X-ray Spectrometry*, 1997, 26, 359.
15. S. Della Longa, S. Pin, R. Cortes, A.V. Soldatov, B. Alpert, *Biophys. J.*, 1998, 75, 3154.